Supporting Information for

Machine-learning-driven global exploration reveals atomic-scale degradation of $LiNiO_2$ during delithiation

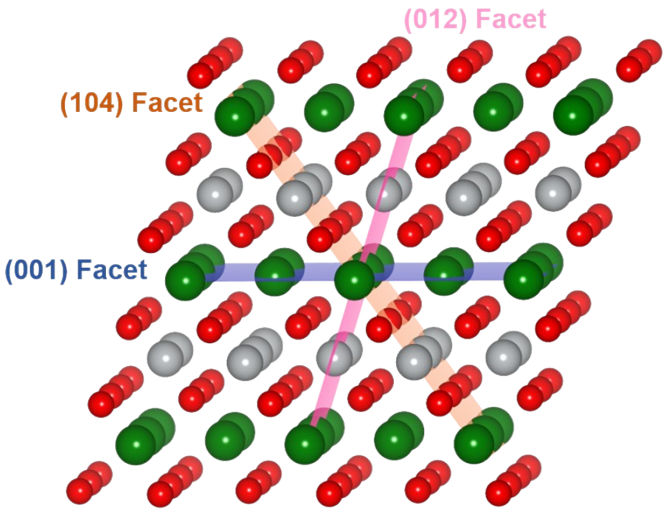

Figure S1. Section of the layered $LiNiO_2$ structure highlighting the three investigated surface facets, (001), (012), and (104). Blue, pink, and orange represent the (001), (012), and (104) planes, respectively.

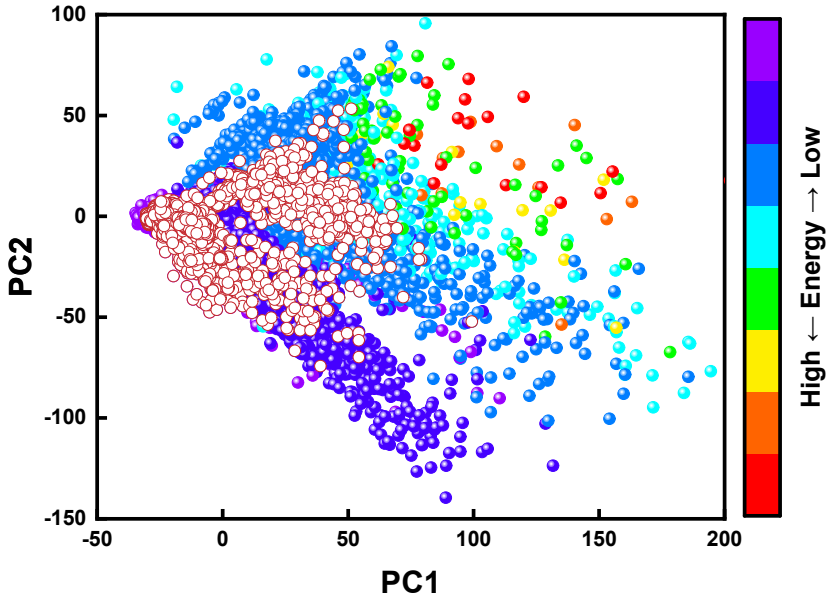

Figure S2. PCA analysis of the datasets from $LiNiO_2$ potential. The energy of each data point is colored. The region marked by red circles represents the highly delithiated Li_xNiO_2 ($x < 0.2$) structures.

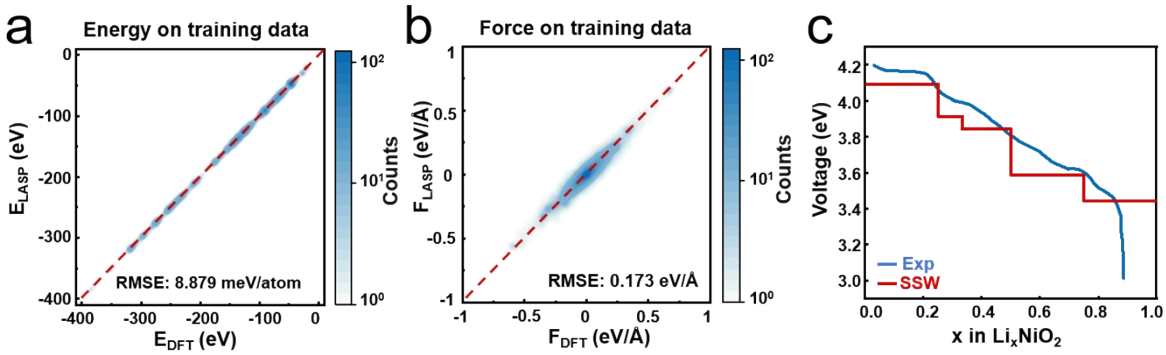

Figure S3. (a-b) Energy and force comparisons between DFT and LASP calculations. The root mean square error (RMSE) values are provided in each figure to quantify the accuracy of the LASP relative to the DFT data. **(c)** Voltage profile comparison between SSW and experimental.

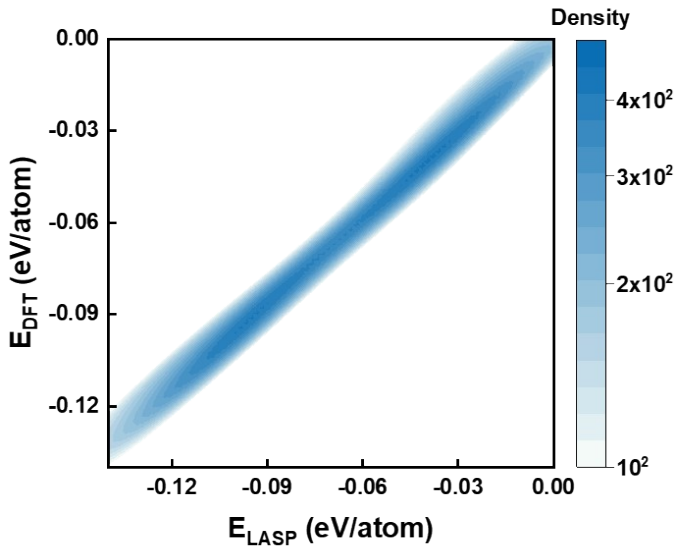

Figure S4. Energy comparisons between DFT and LASP calculations reported in Figure 1.

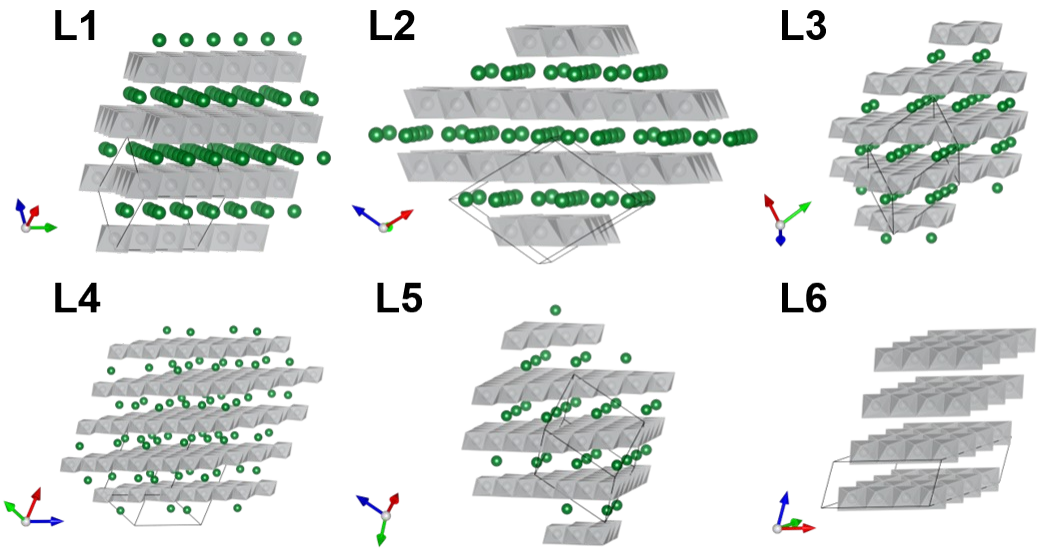

Figure S5. Three-dimensional view of the crystal structures and Li vacancy orderings reported in Figure 1. Li ions are depicted as green spheres, while Ni octahedra are grey. Unit cells have not been standardized.

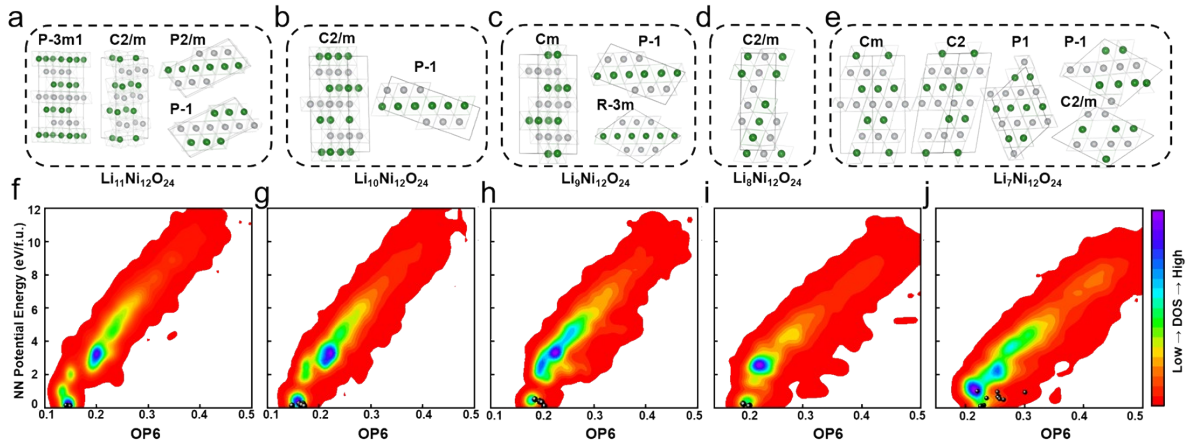

Figure S6. The global potential energy surface (PES) of $Li_xNi_{12}O_{24}$ (x=7-11) as determined from the SSW global search. The energy (eV/f.u.) of the most stable structure is set as the reference zero. The x axis is the comment structure fingerprint for the crystal, namely, the distance-weighted Steinhardt-type order parameter (OP) with different angular moment L = 2,4,6 which can distinguish different minima, and the y axis is the relative energy of minima. Due to the special hexagonal symmetry of $LiNiO_2$, we choose OP6 (L = 6) to distinguish different structures. The lowest energy minima from the SSW trajectories are marked in the global PES with black spheres. On the right side of the figure are the structures of different space groups explored by SSW. Among them, Li ions and Ni ions are represented by green and gray balls respectively. The lattice O ions forming octahedra or tetrahedra are not shown, and the O ions forming oxygen dimers or oxygen are represented by red balls. The black, blue, and red dashed boxes represent the layered structure, the non-layered structure that produces O dimers, and the non-layered structure that produces oxygen, respectively.

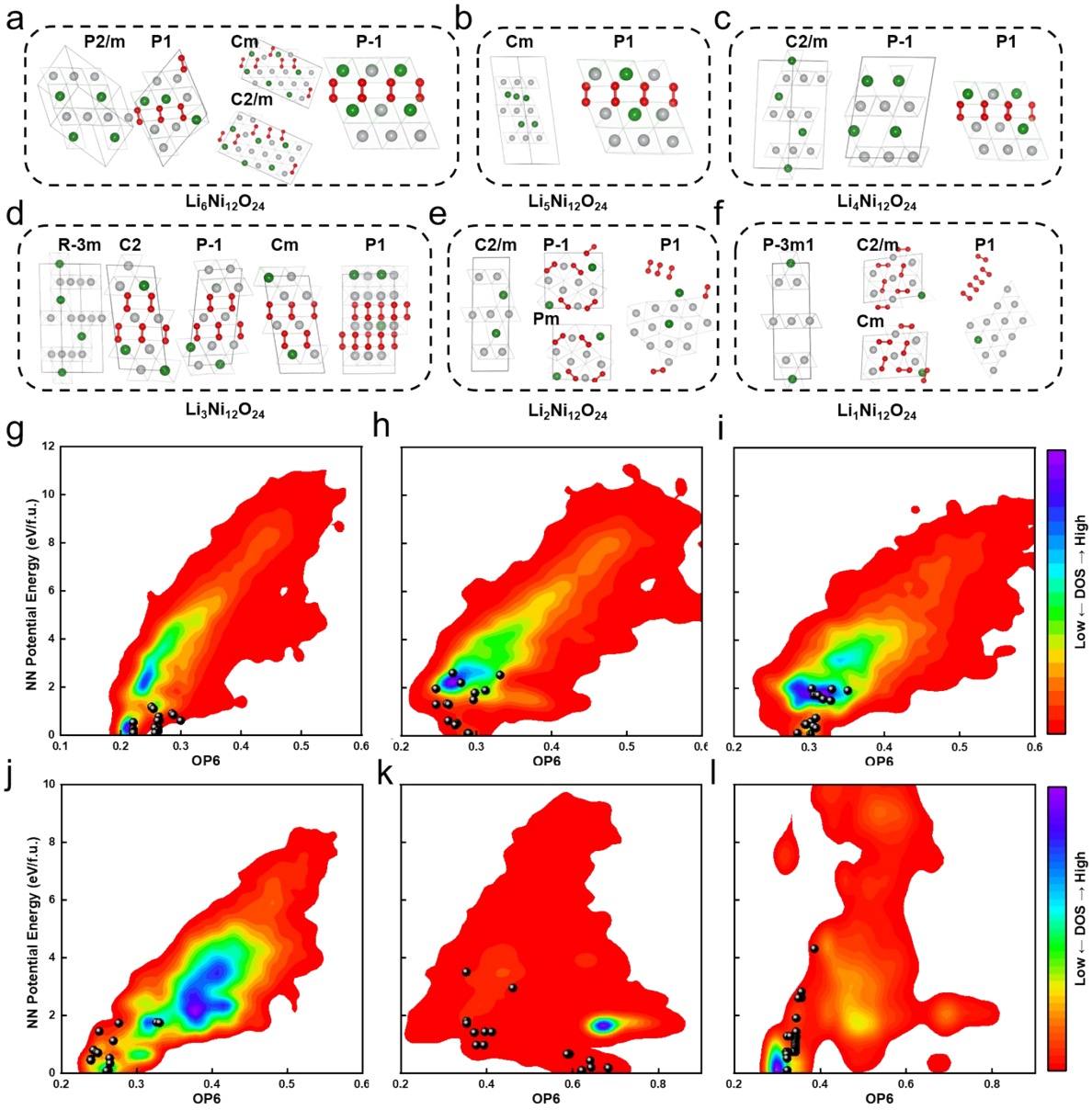

Figure S7. The global PES of $Li_xNi_{12}O_{24}$ (x=1-6) as determined from the SSW global search.

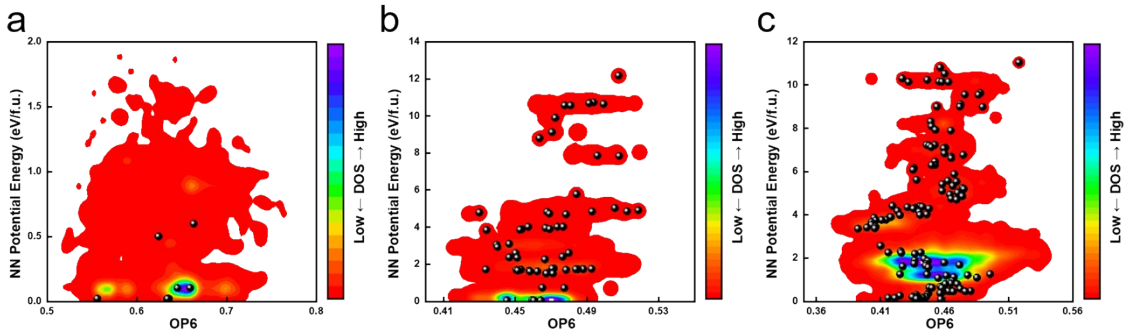

Figure S8. Global PES of (001), (012), and (104) surface of $LiNiO_2$ as determined from the SSW global search.

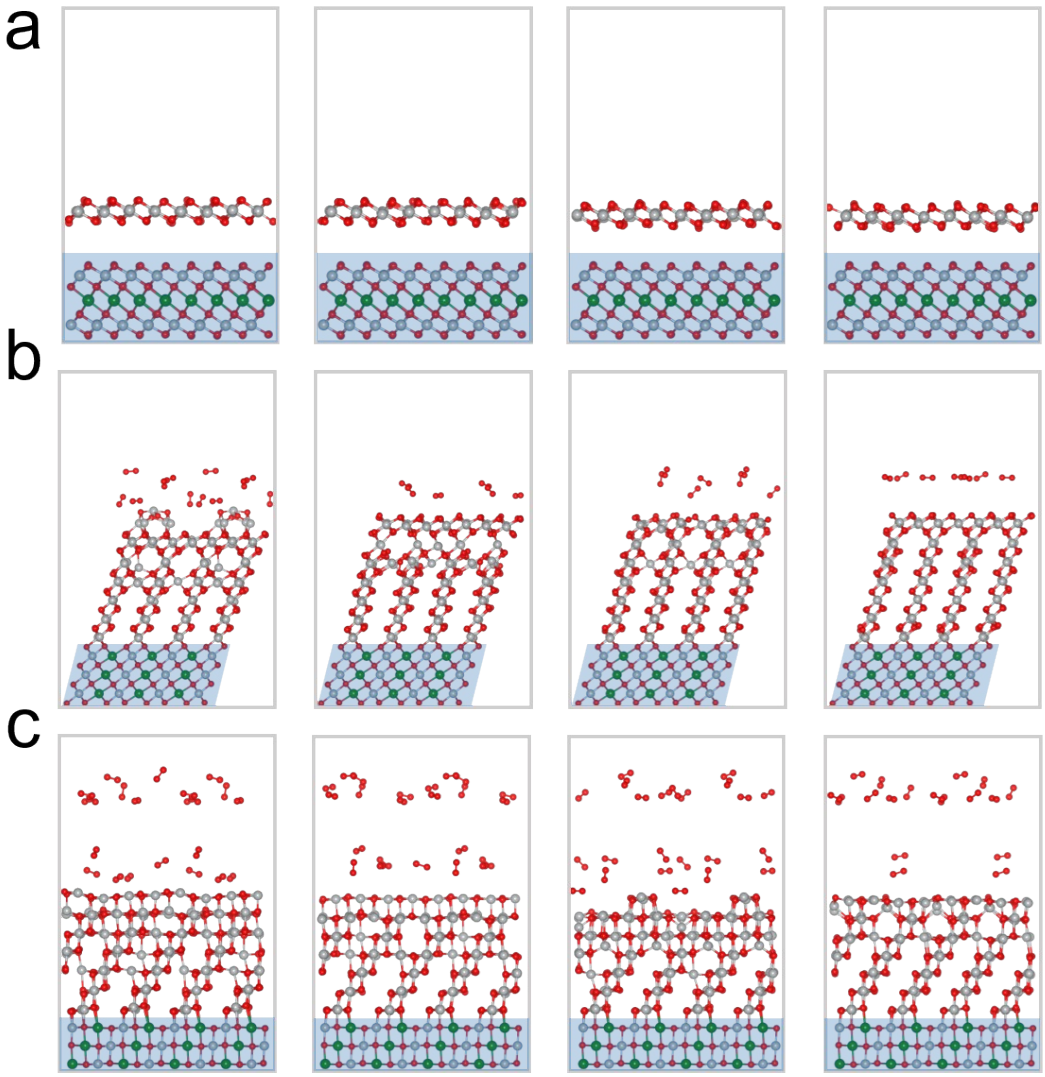

Figure S9. Final configurations of (001), (012), and (104) surfaces after four independent 2 ns molecular dynamics (MD) simulations.

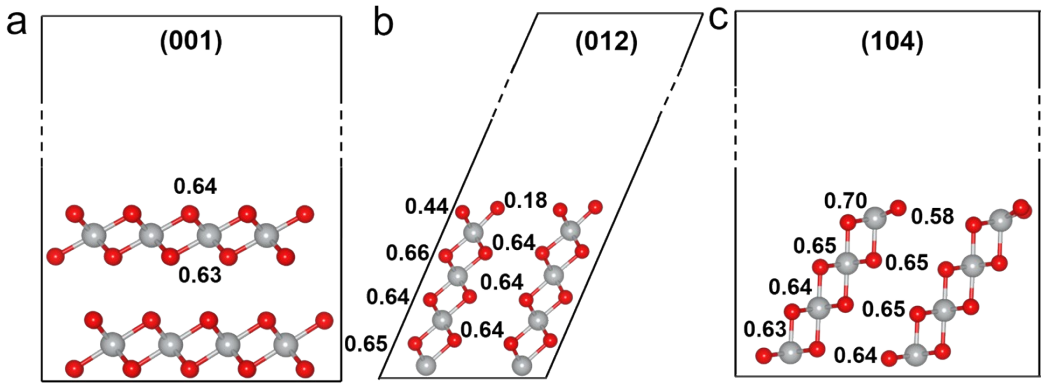

Figure S10. Oxidation states of the O ions on and near the (001), (012), and (104) facets of $LiNiO_2$ according to the Bader charge analysis.

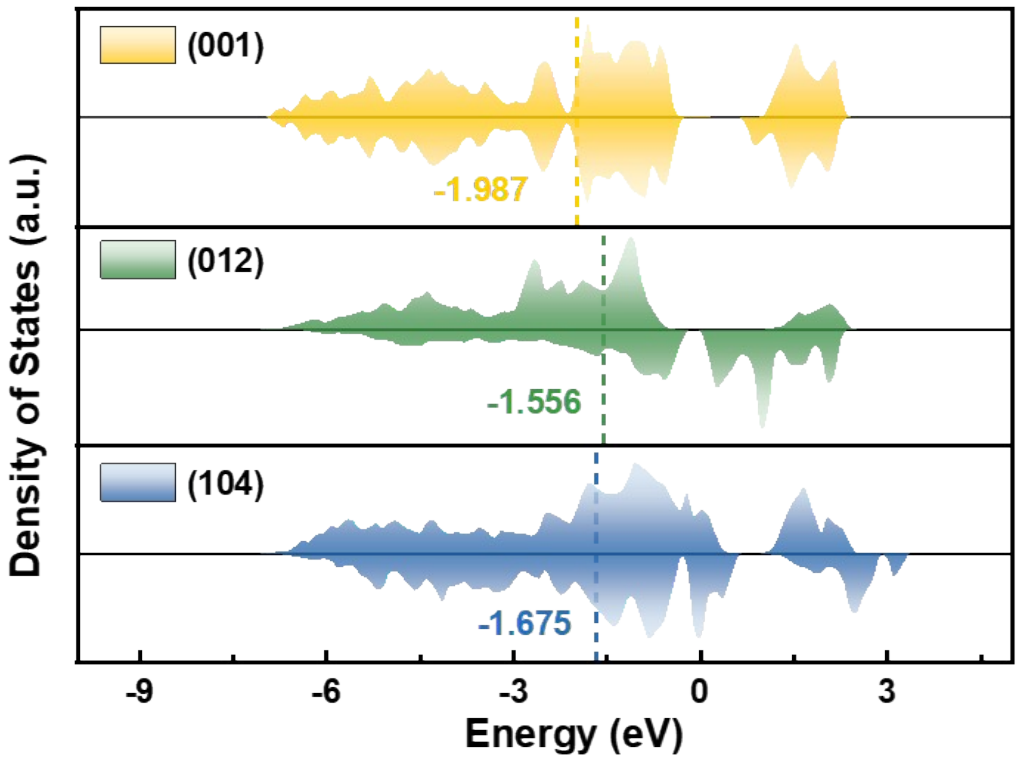

Figure S11. The projected density of states (PDOS) and p-band center of surface oxygen of (001), (012), and (104) surface.

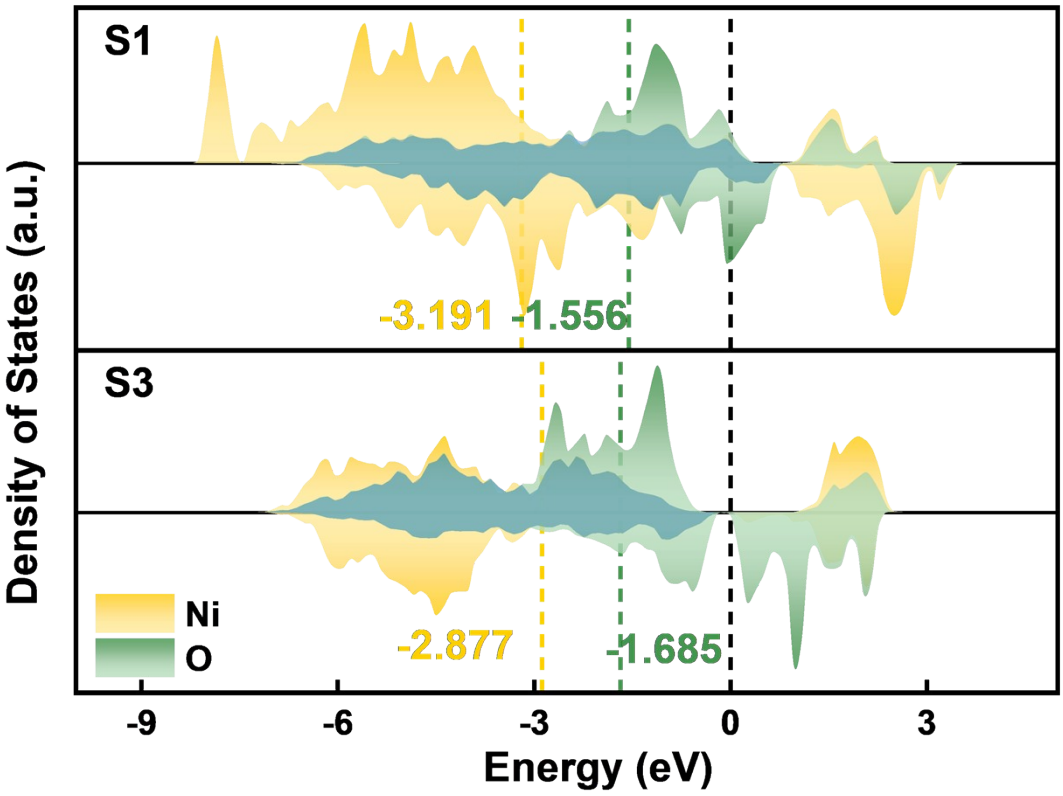

Figure S12. The PDOS and p-band center of surface O ions and d-band center of surface Ni ions of S1 and S3 states from (012) surface.

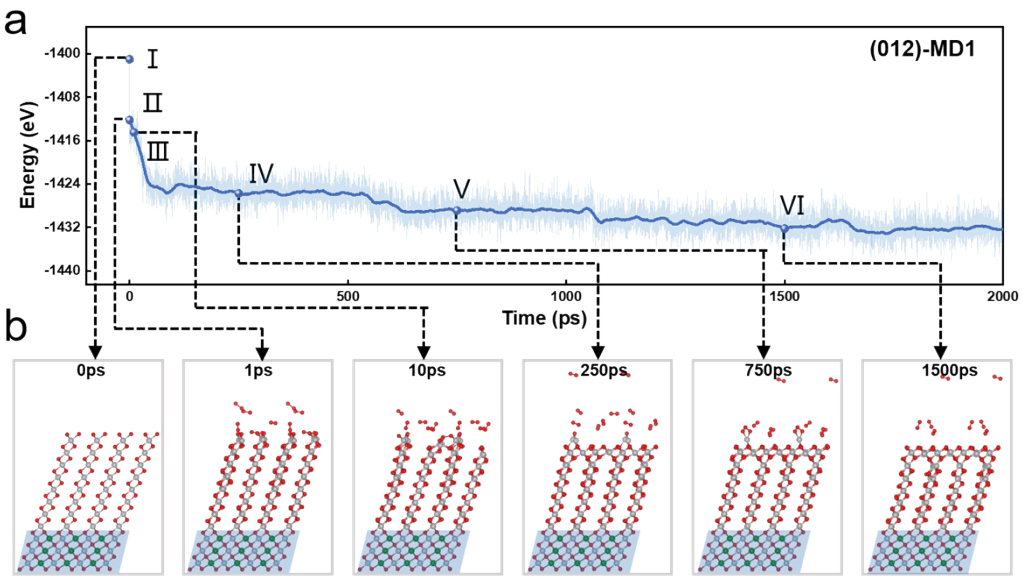

Figure S13. The MD evolution process on the (012) surface from Figure 3c MD-1. (a) The change in total energy with the (104) surface from 2ns MD simulations at 800K. (b) The indicated positions represent the structures extracted for further analysis.

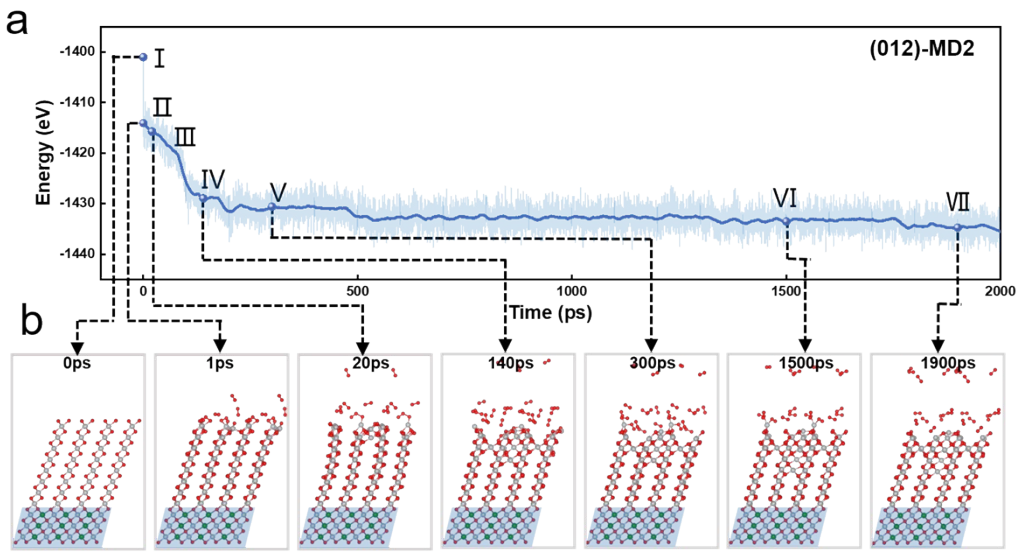

Figure S14. The MD evolution process on the (012) surface from Figure 3c MD-2. (a) The change in total energy with the (012) surface from 2ns MD simulations at 800K. (b) The indicated positions represent the structures extracted for further analysis.

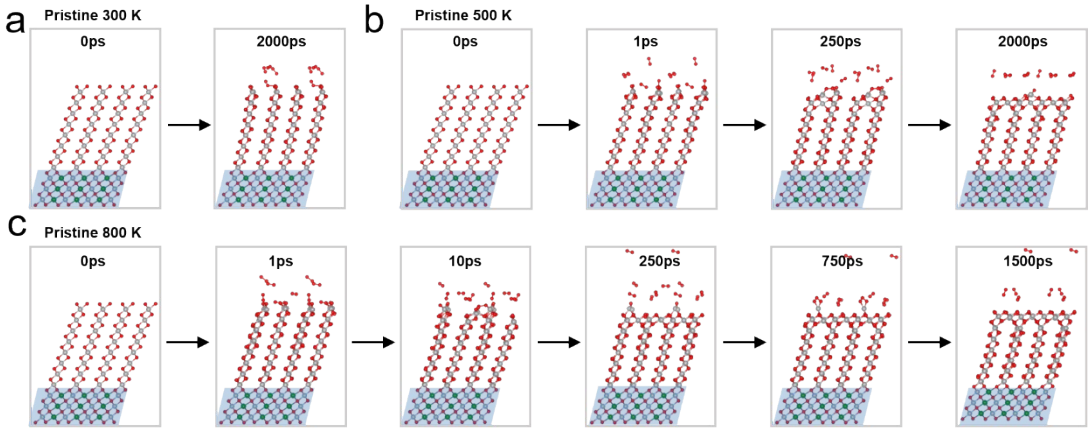

Figure S15. Temperature-dependent MD snapshots of the highly delithiated $LiNiO_2$ (012) surface at 300 (a), 500 (b), and 800 K (c).

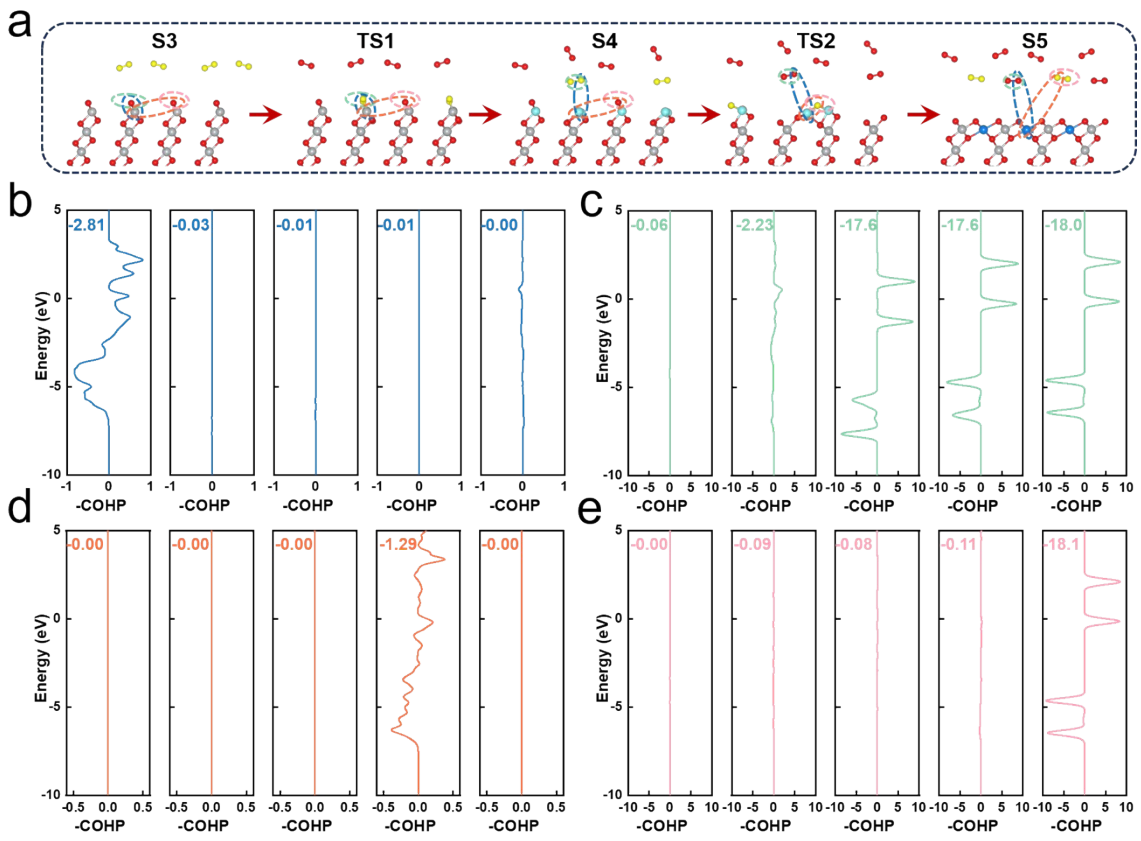

Figure S16. Crystal orbital Hamiltonian population (COHP) analysis of Ni-O and O-O bonding changes during the structural rearrangement mechanism identified by DESW simulations from Path II-1. Structure (a) represents S3, TS1, S4, TS2, and S5 in Path II-1 from Figure 3d. The COHP of the corresponding structures are shown in Figures (b-e). During the two processes of S3→TS1→S4 and S4→TS2→S5, the Ni-O bond breaks, and the O ions after the breakage approach each other to form O_2. The blue and orange dashed circles represent different Ni-O bonds in each state, while the green and pink represent different O-O bonds.

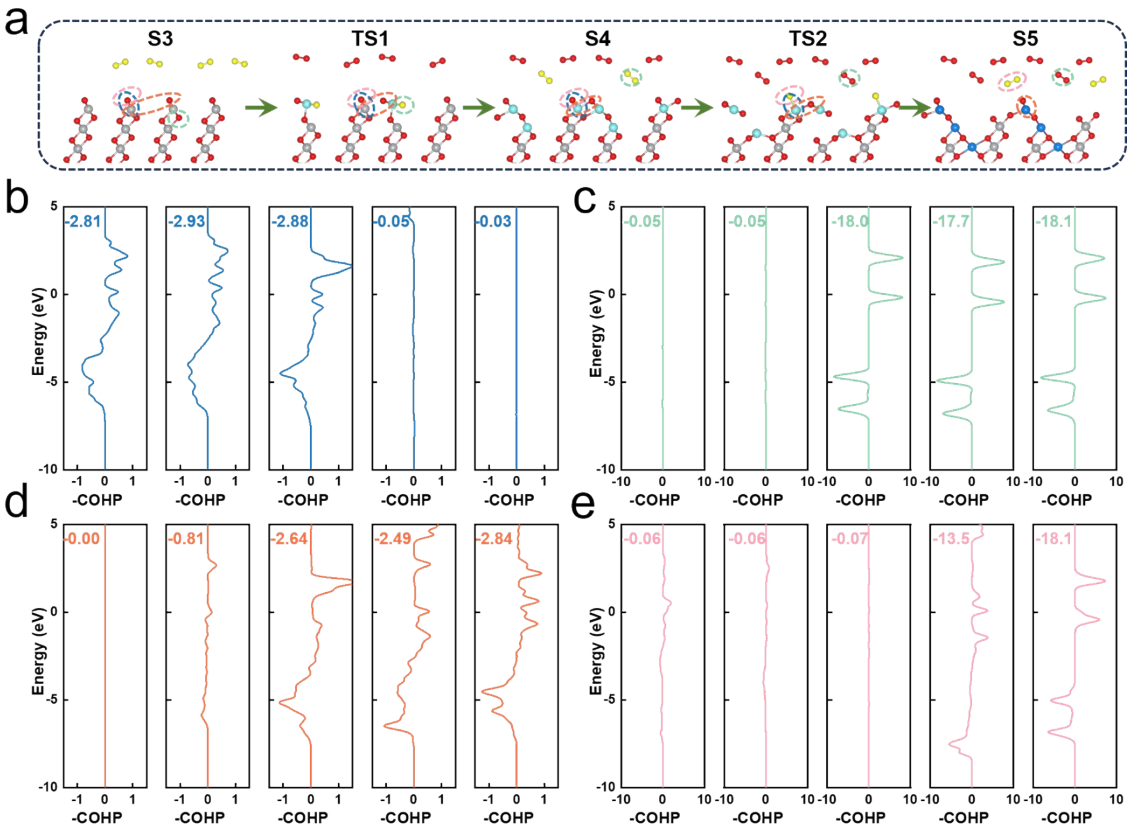

Figure S17. COHP analysis of Ni-O and O-O bonding changes during the structural rearrangement mechanism identified by DESW simulations from Path II-2. Structure (a) represents S3, TS1, S4, TS2, and S5 in Path II-2 from Figure 3d. The COHP of the corresponding structures are shown in Figures (b-e). During the two processes of S3→TS1→S4 and S4→TS2→S5, the Ni-O bond breaks, and the O ions after the breakage approach each other to form O_2. The blue and orange dashed circles represent different Ni-O bonds in each state, while the green and pink represent different O-O bonds.

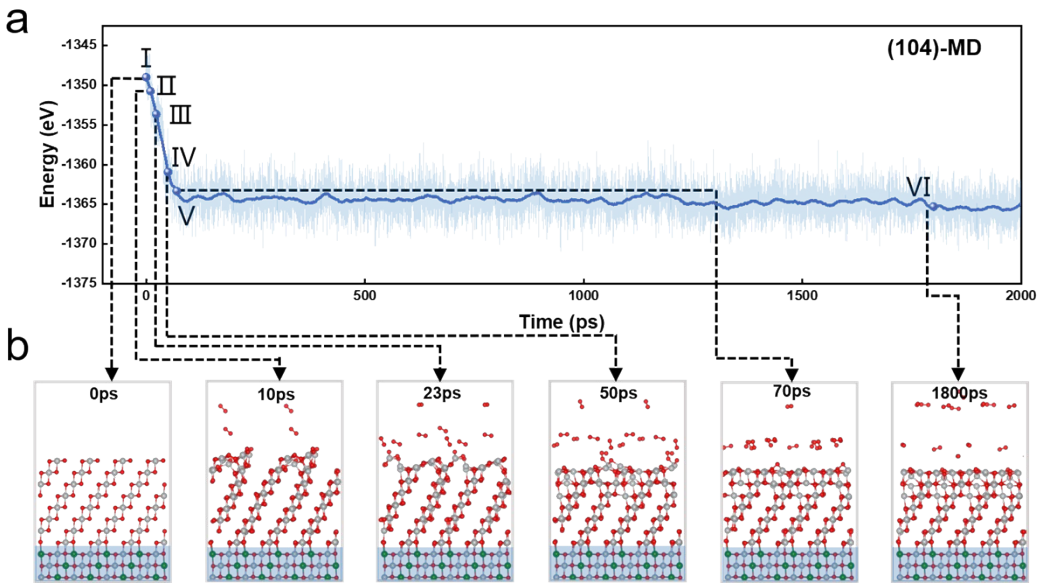

Figure S18. The MD evolution process on the (104) surface from Figure 4c. (a) The change in total energy with the (104) surface from 2ns MD simulations at 800K. (b) The indicated positions represent the structures extracted for further analysis.

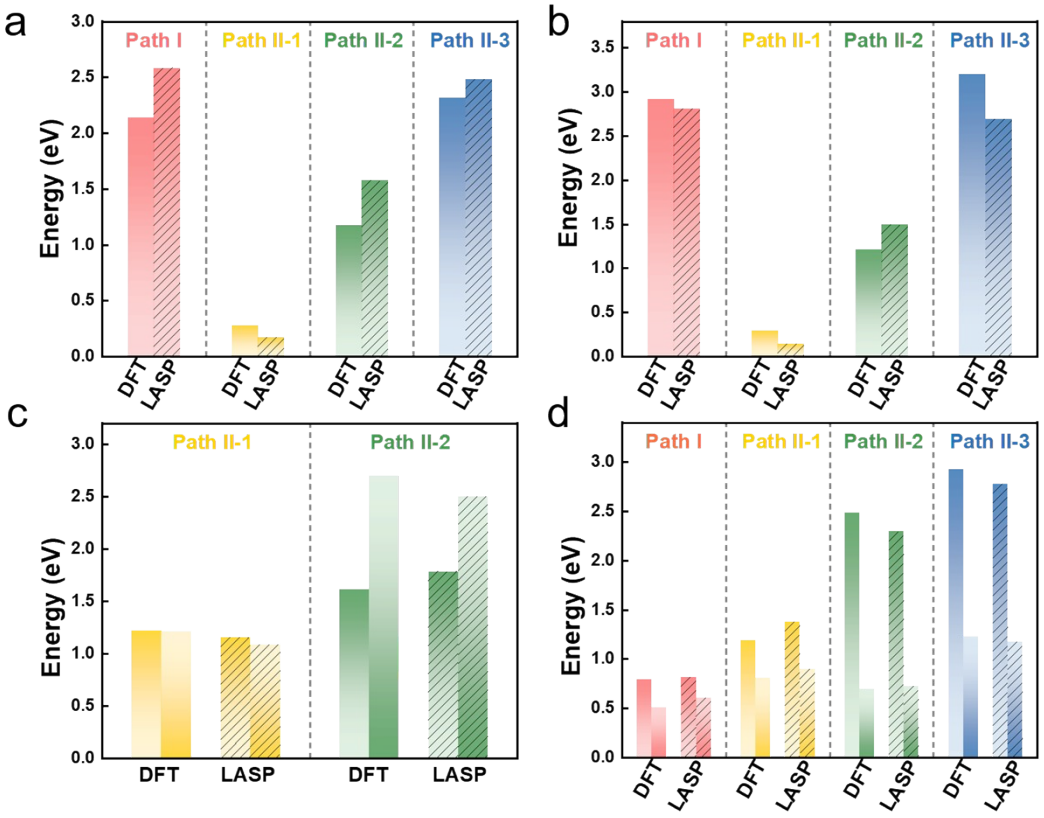

Figure S19. Energy barriers comparisons between DFT and LASP calculations reported in Figure 2-4.

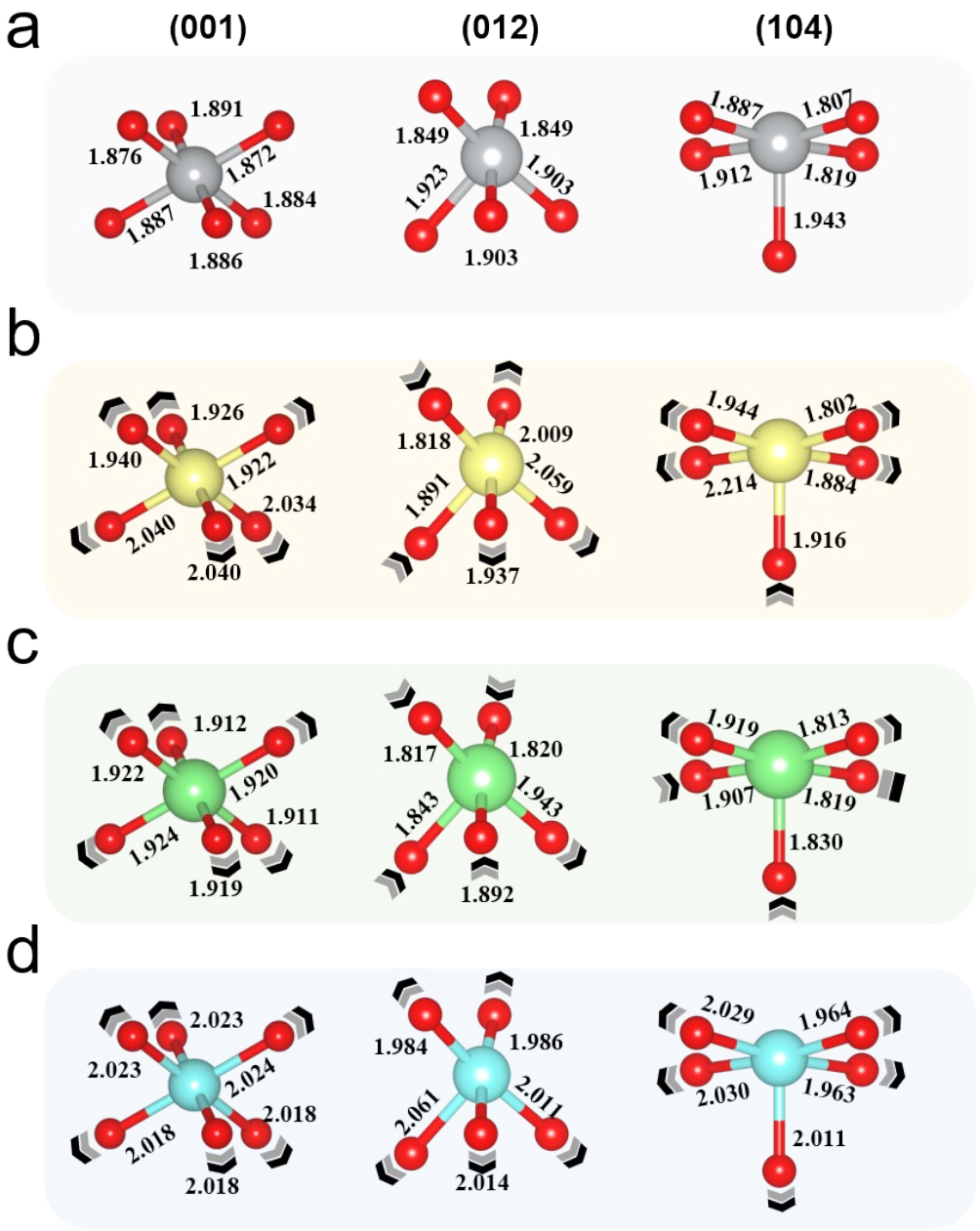

Figure S20. Bond lengths evolution showing Ni (gray), Ti (yellow), Al (green), Mg (blue), and O (red) atomic positions.

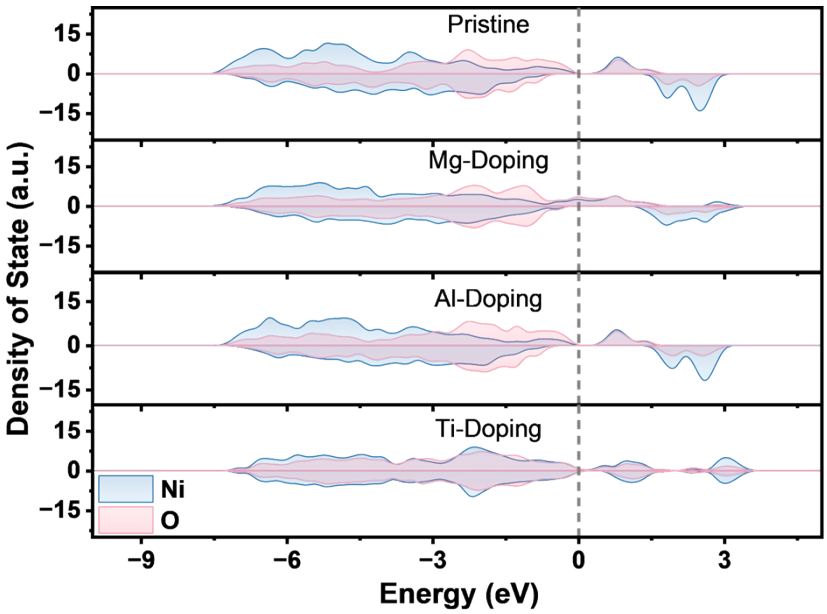

Figure S21. PDOS onto Ni and O orbitals for pristine and Mg-, Al-, and Ti-doped bulk $LiNiO_2$.

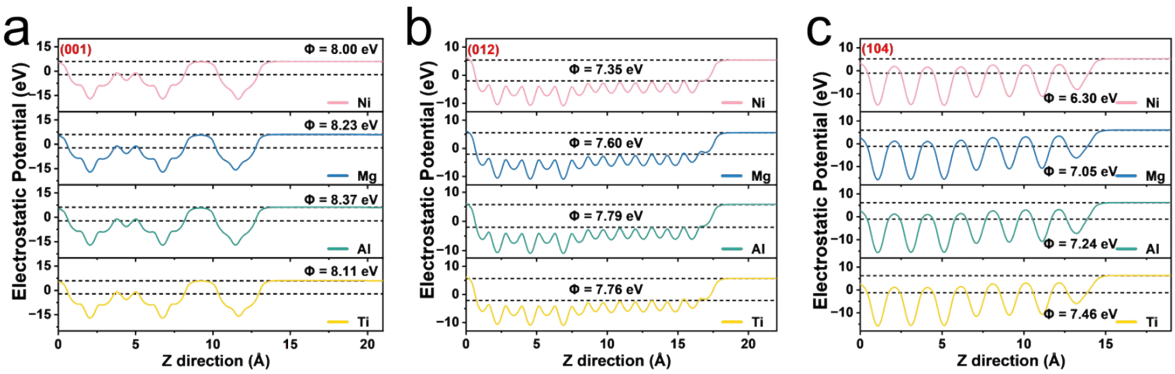

Figure S22. Planar-averaged electrostatic potential profiles along the surface-normal direction and calculated work functions of pristine and Mg-, Al-, and Ti-doped $LiNiO_2$ (a) (001), (b) (012) and (c) (104) surfaces.

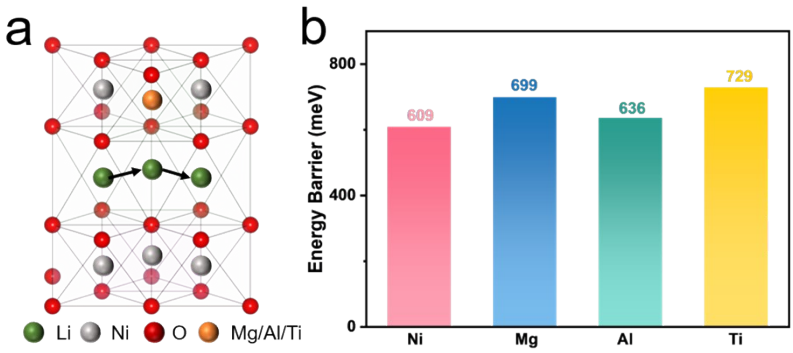

Figure S23. Li migration behaviors in pristine and Mg-, Al-, and Ti-doped bulk $LiNiO_2$. (a) Schematic illustration of the Li migration octahedral-tetrahedral-octahedral pathway. (b) Energy barriers for Li migration obtained from climbing-image nudged elastic band calculations.